IOPscience iopscience.iop.org

Home Search Collections Journals About Contact us My IOPscience

Structure of Fe–Co/Pt(001) superlattices: a realization of tetragonal Fe–Co alloys

This article has been downloaded from IOPscience. Please scroll down to see the full text article.

2007 J. Phys.: Condens. Matter 19 016008

(http://iopscience.iop.org/0953-8984/19/1/016008)

View the table of contents for this issue, or go to the journal homepage for more

Download details:
IP Address: 129.252.86.83
The article was downloaded on 28/05/2010 at 15:02

Please note that terms and conditions apply.

INSTITUTE OF PHYSICS PUBLISHING JOURNAL OF PHYSICS: CONDENSED MATTER

J. Phys.: Condens. Matter **19** (2007) 016008 (13pp) doi:10.1088/0953-8984/19/1/016008

Structure of Fe–Co/Pt(001) superlattices: a realization of tetragonal Fe–Co alloys

G Andersson[1], M Björck[1], H Lidbaum[2], B Sanyal[1], C Chacon[1,4], C Zlotea[3,5] and S Valizadeh[2]

[1] Department of Physics, Uppsala Universitet, Box 530, SE-75121 Uppsala, Sweden
[2] Department of Engineering Sciences, Uppsala Universitet, Box 534, SE-75121 Uppsala, Sweden
[3] Department of Materials Chemistry, Uppsala Universitet, Box 538, SE-75121 Uppsala, Sweden

E-mail: gabriella.andersson@fysik.uu.se

Received 5 July 2006, in final form 16 November 2006
Published 7 December 2006
Online at stacks.iop.org/JPhysCM/19/016008

Abstract

The structural properties of a tetragonally distorted $Fe_{1-x}Co_x$ alloy, in the form of $Fe_{1-x}Co_x$/Pt(001) superlattices with $x = 0.64$, have been investigated experimentally. The study follows recent theoretical predictions on the enhanced uniaxial magnetocrystalline anisotropy of such alloys with specific combinations of chemical composition and tetragonal distortion. The ratio between out-of-plane and in-plane lattice parameters in the $Fe_{0.36}Co_{0.64}$ layers, c/a, was found to vary between 1.18 and 1.31, depending on the thickness ratio between the alloy and the spacer. This covered the range of interest $c/a = 1.20$–1.25 in the previous calculations and should be compared to $c/a = 1$ in the original bcc alloy lattice. Simulations of x-ray diffraction patterns as well as density functional calculations support the derivation of the $Fe_{0.36}Co_{0.64}$ lattice parameters.

1. Introduction

Storage densities in magnetic hard drives have increased dramatically during the past decades. This increase has mainly been achieved through diminishing the bits recorded in the storage layer [1]. However, when the recording medium grain volume decreases beyond the limit when the magnetic energy per grain becomes comparable to the thermal energy $k_B T$, one has reached the onset of the superparamagnetic effect. The recorded data will then not be stable over time, but will be erased by thermal fluctuations [1, 2]. A means by which to push the grain volume limit further [3] is the use of materials with high values of K_u, the intrinsic uniaxial magnetocrystalline anisotropy energy, since the magnetic energy is proportional to K_u. In

[4] Present address: Matériaux et Phénomènes Quantiques, Université Paris 7, CNRS, UMR 7162, 2 Place Jussieu, 75251 Paris Cedex 5, France.
[5] Present address: European Commission—DG JRC, Institute for Energy, Clean Energies Unit, PO Box 2, NL-1755 ZG Petten, Netherlands.

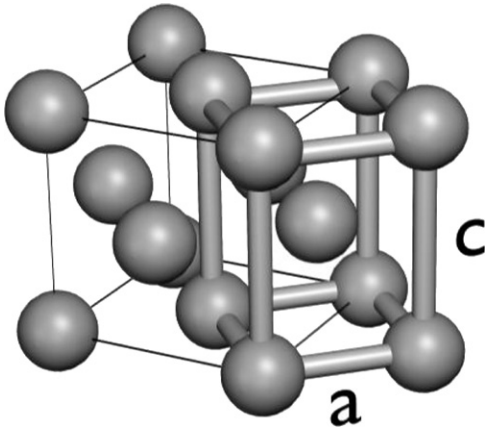

Figure 1. Artistic view of the entwined bct (thicker lines) and fct (thinner lines) unit cells. The bct in-plane atomic distance a, which will be used throughout the text, is defined as shown in the picture. If $c/a = 1$, the bcc lattice is obtained.

addition, a large saturation magnetization, M_s, of the recording medium increases the field available for reading the data and reduces the required write field, $H_w \approx K_u/M_s$, which is to be delivered by the writing head. Hence, large K_u and M_s values are highly desired properties of future high-density magnetic recording materials.

In recent theoretical papers [4, 5] highly interesting properties of Fe–Co alloys with body centred cubic and tetragonal structures are proposed. Of particular interest for recording applications is the actual achievement of combined large values of both K_u and M_s, and in addition a flexibility in tuning the magnetocrystalline anisotropy energy through the alloy composition, with maximum K_u occurring around 60 at.% Co. An advantage when comparing to the extensively studied $L1_0$ FePt alloys [6, 7] is the considerably lower deposition temperatures for Fe–Co alloys (around 400–500 K), although fabrication of FePt and CoPt alloys under somewhat improved conditions has recently been demonstrated [8, 9].

Recently we have presented promising preliminary experimental results on the magnetocrystalline anisotropy energy of tetragonally strained Fe–Co alloy layers in the form of a Fe–Co/Pt superlattice [10]. In the present paper we report on the detailed structural properties of a series of such Fe–Co/Pt superlattices with varying tetragonal strain but constant alloy composition. The platinum layers, with face centred cubic (fcc) structure in the bulk metal, here play the role of compressing the originally body centred cubic (bcc) [11] Fe–Co alloy in the in-plane directions. This results in a tetragonally distorted lattice through the elastic response, which increases the lattice parameter in the out-of-plane direction. Previous investigations of Fe/Pt multilayers [12–15] in some cases concluded that the Fe layers attained an fcc structure when the layers were thinner than approximately 8 Å [12, 14], whereas thicker Fe layers became bcc with a 45° rotation with respect to the Pt layers [13, 15]. Both cases can be accomodated in a single picture by viewing the Fe lattice as body centred tetragonal (bct), i.e. originally a bcc structure which is tetragonally deformed through compressive biaxial in-plane strain (cf Bain distortion), as shown in figure 1. The ratio c/a between the out-of-plane and in-plane bct lattice parameters then gives the degree of tetragonal distortion. Following this line of reason, $c/a = 1$ and $\sqrt{2}$ correspond to the pure bcc and fcc structures, respectively. We will regard the crystal structure of the Fe–Co/Pt superlattices as bct throughout this paper, and consequently use the interatomic distances c and a as defined in figure 1.

Table 1. The Fe–Co/Pt multilayers prepared for the study, with their nominal and measured bilayer thickness, Λ, and number of repetitions, N. The experimental Λ was obtained from the x-ray reflectivity results. The sample label refers to the Fe–Co thickness in monolayers, n_{FC}, and the Pt thickness in monolayers, n_{Pt}. Individual layer thicknesses (L_{FC}, L_{Pt}) are nominal. For details, see text.

n_{FC}/n_{Pt}	L_{FC} (Å)	L_{Pt} (Å)	Nom. Λ (Å)	Exp. Λ (Å)	N
3/3	4.3	5.9	10.2	9.5	40
5/5	7.1	9.8	16.9	16.3	24
8/8	11.4	15.7	27.1	26.6	25
3/7	4.3	13.7	18.0	17.5	23
4/6	5.7	11.8	16.5	16.7	23
6/4	8.5	7.8	16.3	16.2	25
7/3	9.9	5.9	15.8	15.5	26
8/6	11.4	11.5	22.9	22.3	30
6/9.5	8.5	18.6	27.1	27.0	25

Straightforward variation of the strain state in superlattice structures is accomplished through varying the individual layer thickness of the constituents. Different thickness combinations predominantly influence the out-of-plane parameter c, since the in-plane parameter a is controlled to a large extent by the substrate and buffer layer. As will be shown, minor variations in a with superlattice composition are observed.

In order to focus the scope of the present paper, details on the magnetic properties of the samples will be published elsewhere [16]. Preliminary results on the general trend in the dependence of K_u on the strain state were presented in our previous paper [10].

2. Experimental details

The multilayers were grown by dc magnetron sputtering in ultrahigh-vacuum (UHV)-based equipment, described in detail elsewhere [17], with a base pressure below 1×10^{-7} Pa and Ar (99.9999%) as the sputtering gas. The purity of each target was 99.95% for Fe, 99.95% for Co and 99.99% for Pt, respectively. Substrates of MgO were used, $10 \times 10 \times 0.5$ mm^3, with edges along [100] and [010] directions and the [001] direction perpendicular to the polished surface. Each substrate was annealed at 700 °C for 15 min before cooling to the buffer layer growth temperature, which was 330 °C [14, 17]. The temperature was allowed to stabilize for at least 30 min before the buffer layer was deposited. The buffer consisted of 6 Å of Fe (4 ML) covered by 39 Å of Pt (20 ML) [14, 18]. Deposition rates at an Ar pressure of 0.8 Pa were typically 0.45 and 0.79 Å s^{-1} for pure Fe and Pt, sputtered with 50 and 30 W magnetron power, respectively. After the buffer deposition the temperature was decreased to 200 °C, which was found to give better crystallinity and sharper interfaces than the lower temperatures reported previously for Fe/Pt epitaxial multilayers [13, 14].

The growth was then continued with the Fe–Co/Pt bilayers, repeated N times, with N chosen to make the total film thickness comparable for all samples. The final layer was always 15 Å of Pt to enhance the protection against oxidation, regardless of the nominal Pt thickness, L_{Pt}, in the rest of the superlattice. The set of samples prepared is presented in table 1.

In the following, subscripts for quantities referring to the Fe–Co alloy will be 'FC', whereas 'Pt' will refer to the Pt layers of the multilayer structure. Different samples will be referred to by their label n_{FC}/n_{Pt}, indicating the nominal number of monolayers of each constituent: 1 ML of Fe–Co corresponded nominally to 1.414 Å [19], and 1 ML of Pt was

set to be 1.962 Å [20] in the deposition procedure. The choice of thickness combinations was made to cover both a constant strain state, given by n_{FC}/n_{Pt}, and a constant interface density, given by $1/(n_{FC} + n_{Pt})$, while varying the relative amount of Fe–Co in the multilayers. Two of the samples, 8/6 and 6/9.5, contribute with additional strain states for two n_{FC} values. In addition, the 6/9.5 sample has the same interface density per unit thickness as the 8/8 sample.

The sputtering yield scales approximately linearly with the magnetron power. Hence, the composition of the Fe–Co alloy was regulated through the power on the Fe and Co targets, respectively, during co-sputtering. Since the predicted strong enhancement of K_u occurs at approximately 60 at.% Co [5], this composition was chosen for the present sample series. Obtained from the relative rates of Fe and Co, the power used was 20 W on the Fe target and 40 W on the Co target. This resulted in a total deposition rate of typically 0.52 Å s^{-1}. The exact rates for each step in the sputtering procedure were obtained from x-ray diffraction on calibration samples consisting of sandwiches of two superlattices. When producing these calibration samples the deposition time of one of the constituents was changed from the first to the second superlattice, while the time of the other constituent was kept constant. In addition, a film of 1000 Å of Fe–Co was grown under the same conditions as the multilayers in order to provide a reference for, e.g., lattice parameters and the alloy composition. The buffer layer in that particular sample was 45 Å of Fe, deposited at 330 °C, and the film was capped by 20 Å of Pt.

2.1. Characterization methods

The chemical composition of the alloy was established through Rutherford backscattering spectrometry (RBS) and x-ray photoelectron spectroscopy (XPS) on the 1000 Å Fe–Co film. The RBS measurements were performed using 2.00 MeV He^+ ions at the Tandem accelerator laboratory in Uppsala. The RBS yield for a total dose of 10 μC was analysed using the RUMP software [21]. The XPS measurements, using Al Kα radiation, were performed at two different positions on the sample. Depth concentration profiles were created through measuring the Fe and Co 3p peaks, the Pt 4f peak and the O 1s peak between ten sputtering cycles of 30 s each. The energy scale was calibrated from measurements on pure Fe and Co target material.

The structure of the multilayers was investigated through x-ray reflectivity and diffraction (XRD) in various configurations. For reflectivity, θ–2θ scans and rocking curves (ω scans), a Bruker D5000 diffractometer was used in Bragg–Brentano geometry with Cu Kα radiation ($\lambda = 1.541$ Å). The combined reflectivity and diffraction scans covered the angular range $2\theta =$ 1°–90°, including the MgO(002) Bragg peak at $2\theta \approx 42.9°$. Rocking curves were measured at the 2θ value corresponding to the average (002) atomic plane distance, i.e. the fundamental superlattice peak. Since the ratio of out-of-plane to in-plane lattice parameters, c/a, is the most relevant parameter in these samples [5], reciprocal space mapping (RSM) was performed using a Philips X'Pert diffractometer, also operating with Cu Kα x-rays. These RSM scans were performed around the (002), (103) and (204) diffraction peaks, where the Miller indices refer to the directions defined by the bct superlattice. The epitaxial relationship between the substrate and the strained fcc Pt buffer [12] is Pt[100] ∥ MgO[100] and Pt[001] ∥ MgO[001]. The bct Fe–Co/Pt superlattice is then rotated by 45° with respect to the MgO and Pt buffer: the superlattice [100] and [010] directions are parallel to the substrate diagonals. Before the RSM measurements, each sample was aligned using the MgO (002) and (113) diffraction peaks.

Two samples with different nominal layer thicknesses of Pt (6/4 and 6/9.5) were also studied using transmission electron microscopy (TEM). The microscope was a JEOL JEM-2000FXII transmission electron microscope (TEM) operated at 200 kV. Dimple grinding and argon ion etching were used for the preparation of cross-sectional samples.

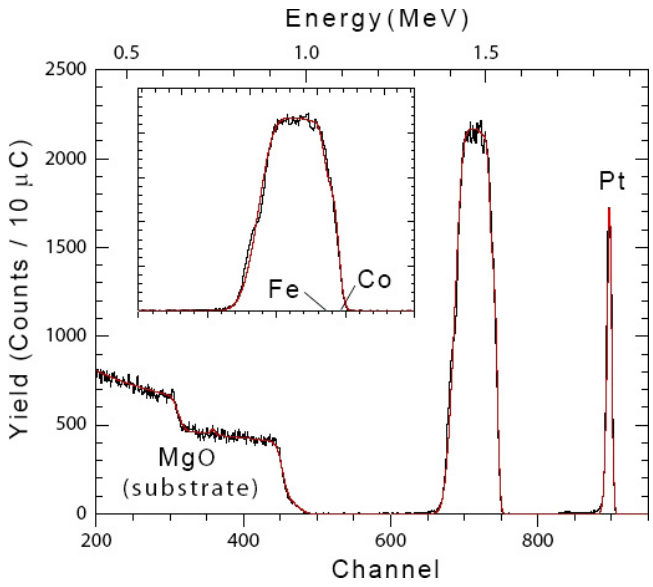

Figure 2. RBS spectrum recorded on the 1000 Å FeCo film, together with the simulation for a composition of 62 at.% Co and 38 at.% Fe. The peak at 1.4–1.5 MeV, enlarged in the inset (channels 600–800), is the FeCo overlayer. The Pt cap is at 1.85 MeV, whereas the feature to the left is the MgO substrate.

(This figure is in colour only in the electronic version)

3. Results

3.1. Chemical composition

The results from the fitting of the RBS data [21] are shown in figure 2. The Fe and Co peaks overlap significantly, as can be seen in the enlarged inset, due to their similar atomic mass. There are, however, features at the edges of the combined peak that can only be reproduced by a Co content of 62 ± 3 at.%. The same value, 66 ± 5 at.% Co, was obtained from XPS. Thus the resulting average composition, 64 ± 5 at.% Co, is close to the 60 at.% Co we aimed for. Both RBS and XPS measurements also prove that there is no oxygen inside the film, and that the Pt cap does not intermix heavily with the FeCo film: within the depth resolution of the two methods there is no detectable mixing. Throughout the remainder of this paper 'FeCo' will be used to denote the $Fe_{0.36}Co_{0.64}$ alloy, unless otherwise stated.

3.2. Structural properties

Examples of θ–2θ XRD scans for samples 6/4, 5/5 and 4/6 are shown in figure 3. The selected samples illustrate the change in the out-of-plane lattice parameter with varying n_{FC}/n_{Pt} while the interface density, $1/(n_{FC} + n_{Pt})$, is kept constant. The x-ray reflectivity data were primarily used to investigate the interface quality as well as the individual layer thicknesses in the samples, as will be discussed further.

An example of RSM results from the 6/4 sample is shown in figure 4. From the FeCo/Pt(002) XRD peak the average out-of-plane parameter $\langle c \rangle$ was obtained for each sample. The in-plane average interatomic distance, $\langle a \rangle$, was obtained from the combined RSM scans

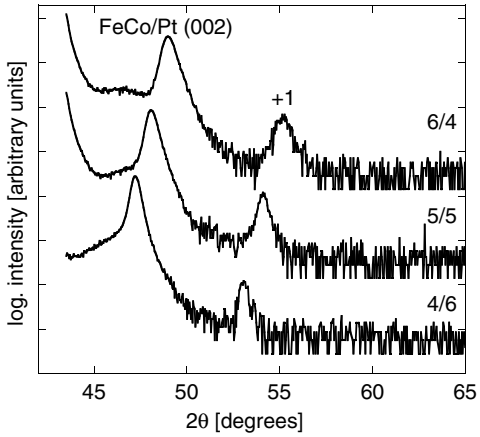

Figure 3. High-angle XRD on samples, from top to bottom: 6/4, 5/5 and 4/6 (scans vertically shifted for clarity). The main Bragg peak, yielding the average (002) plane distance, is indicated, as well as the (+1) satellites arising from the chemical modulation. The large intensity increase on the low-angle side is due to the MgO(002) peak at 42.9°.

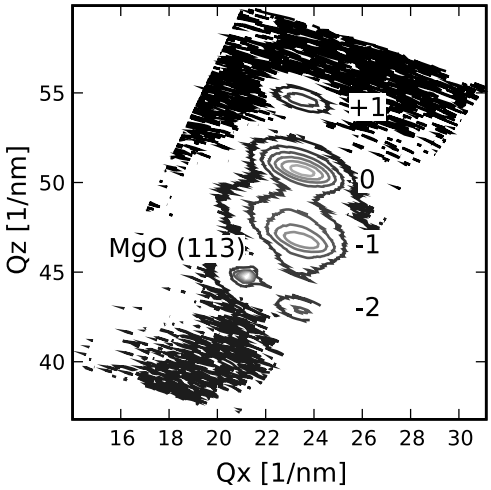

Figure 4. RSM around the (103) Bragg peak of the 6/4 sample. The intensity scale is logarithmic. Note that the MgO(113) peak is not aligned to the scattering plane, hence the suppressed intensity.

around the (002) and (103) and, in some cases, also the (204) Bragg peaks. The Miller indices and lattice parameters refer throughout to the bct structure of the superlattice. Combining two peaks in this way eliminates instrumentation offset errors [22]. Figures 5 and 6 show the changes in the average out-of-plane and in-plane lattice parameters, respectively, with the FeCo content $x_{\mathrm{FC}} = n_{\mathrm{FC}}/(n_{\mathrm{FC}} + n_{\mathrm{Pt}})$, while the interface density is held constant. The variation in $\langle c \rangle$ exhibits the expected Vegard's law behaviour. In figure 6 the lattice parameter as a function of composition of an fcc Fe–Pt alloy is also plotted for comparison. A detailed motivation will be given in the discussion below on structural quality.

A bright-field TEM micrograph of the 6/9.5 sample is shown in figure 7, and figure 8 shows the corresponding selected area electron diffraction (SAED) pattern. Strain within

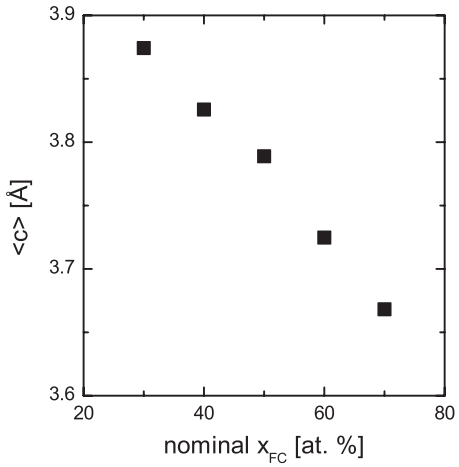

Figure 5. The variation of average out-of-plane lattice parameter, $\langle c \rangle$, with FeCo content, $x_{\mathrm{FC}} = n_{\mathrm{FC}}/(n_{\mathrm{FC}} + n_{\mathrm{Pt}})$, for samples with constant bilayer thickness $n_{\mathrm{FC}} + n_{\mathrm{Pt}} = 10$ ML.

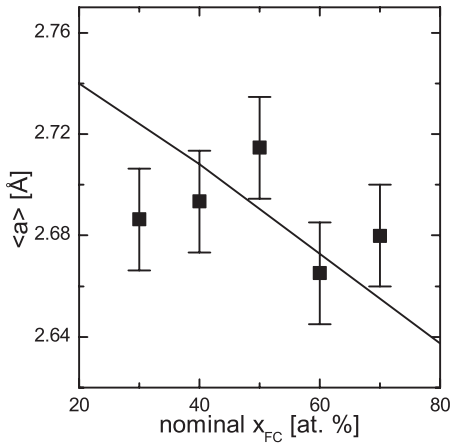

Figure 6. The variation of average in-plane lattice parameter, $\langle a \rangle$, with FeCo content, x_{FC}. Note that the scale is more compressed than in the previous plot. The full line indicates the lattice parameter of an fcc Fe–Pt alloy recalculated to the bct structure. Corresponding bulk values for FeCo and Pt are 2.84 and 2.77 Å, respectively.

the superlattice is observed when comparing the spacing between SAED peaks in directions parallel and perpendicular to the surface. Comparing positions of the superlattice peaks along the MgO [100] and [001] directions of samples 6/4 and 6/9.5 yields average strains within the superlattices of $(0.8 \pm 0.3)\%$ and $(0.1 \pm 0.3)\%$, respectively. These values, which should not be confused with the local strains in the FeCo layers, agree with the results from x-ray measurements. The SAED pattern also shows epitaxial growth of the layers: there is no rotation of the superlattice diffraction spots with respect to the MgO substrate spots. In the bright-field TEM image, contrast from dislocations is visible. The dislocation density and the distribution of local lattice plane orientations will be discussed further in the section on structural quality.

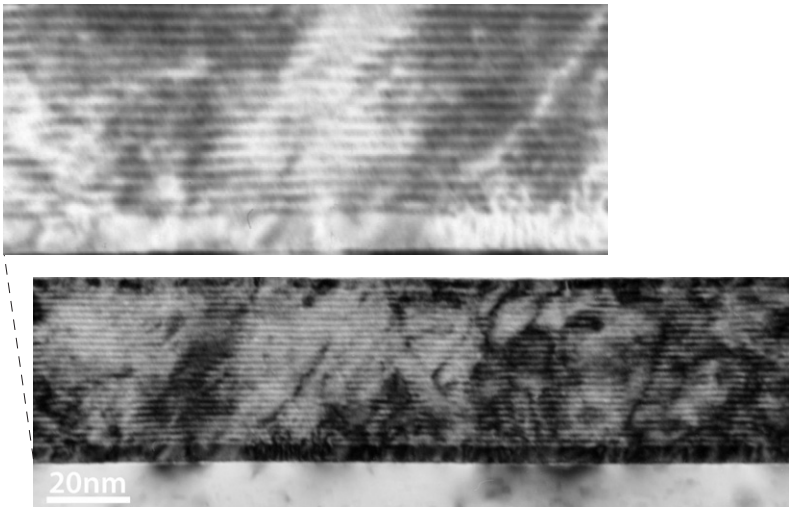

Figure 7. Bright-field TEM micrograph of the 6/9.5 sample. The FeCo layers are brighter and the Pt layers are darker in the bottom (positive) image. In addition, contrast from dislocations within the superlattice is present. In order to increase the contrast from the FeCo and Pt layers, the sample was tilted 3° off the zone axis, although staying parallel to the layers. The top image shows an inverted enlargement of the bottom left corner of the film, where the defects in the Pt buffer layer adjacent to the MgO substrate can be seen more clearly.

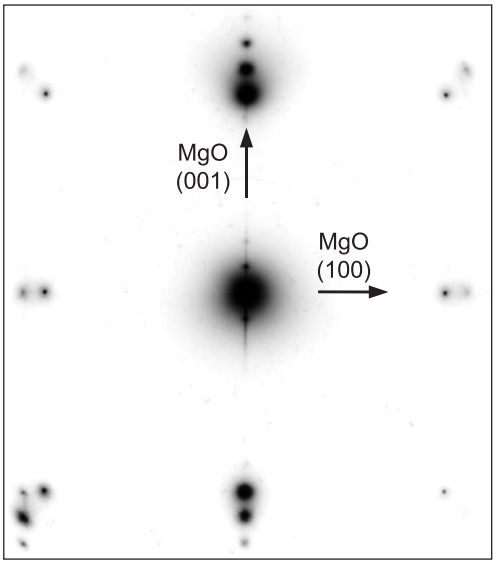

Figure 8. Selected area electron diffraction pattern of the 6/9.5 sample, recorded under identical conditions as the TEM micrograph in figure 7. The superlattice Bragg peaks and satellites are further than the substrate peaks from the central (000) maximum. The arrows indicate the planes of the MgO substrate. Note that the bct superlattice [110] direction is parallel to MgO [100].

4. Discussion

The error bars in the obtained chemical composition of the FeCo alloy are rather large. However, the Co concentration 64 ± 5 at.% is within the region of interest from the point

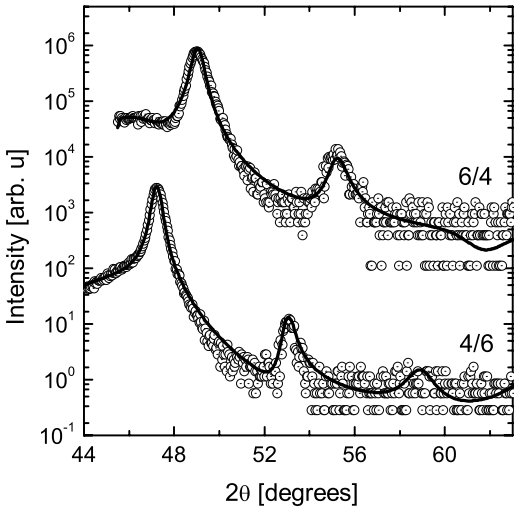

Figure 9. Simulations of the high-angle x-ray diffraction data from the 4/6 and the 6/4 samples (full line) together with the experimental data (circles).

of view of enhanced magnetocrystalline anisotropy [5]. For the analysis of purely structural properties the exact composition is of secondary interest.

4.1. Strain state analysis

We assume in the following discussions that the interatomic distance in the plane is constant throughout each sample, but that it may vary between the different superlattices since it is influenced by the relative amounts of the constituents.

The most straightforward approach to obtain a c_{FC} value is through eliminating a reasonable c_{Pt} from the experimental lattice parameter $\langle c \rangle$, which is a weighted average of c_{Pt} and c_{FC} [23, 24]:

$$\langle c \rangle = \frac{n_{FC} c_{FC} + n_{Pt} c_{Pt}}{n_{FC} + n_{Pt}}. \tag{1}$$

The procedure for deriving the individual lattice parameters c_{Pt} and c_{FC} was the following: a value of c_{Pt} was obtained from the strained $a_{Pt} = \langle a \rangle \sqrt{2}$, assuming a volume-preserving elastic response of the Pt fcc unit cell [25]: $(\Delta c/c_0)_{Pt} \approx -2(\Delta a/a_0)_{Pt}$. This assumption is justified by the structural calculations performed for three different samples, using an electronic band structure method to be described below, and where the Pt unit cell volume change between samples is shown to be negligible. The c_{Pt} values fall in the range 4.1–4.3 Å, in reasonable agreement with the $c_{Pt}^{buf} = 4.16$ Å obtained from XRD on the strained Pt buffer layer. Subsequently the FeCo parameter c_{FC} was calculated using equation (1) with $\langle c \rangle$, c_{Pt} and the nominal relative amounts of FeCo and Pt in the bilayers. The FeCo body centred tetragonal $c/a = c_{FC}/\langle a \rangle$ ratio was finally obtained. Given the above assumptions, the error introduced in the c/a ratio is estimated to be on the order of ± 0.03.

In order to check the validity of the derived model for obtaining the c/a ratio, we have also performed simulations of the high-angle diffraction pattern from the 4/6 and 6/4 samples, according to the model presented in [26]. The simulations are shown in figure 9. They allow the extraction of the individual out-of-plane lattice parameters for the FeCo and Pt layers. Assuming that the layers are homogeneously strained as before, the c/a ratios obtained for

Table 2. c/a values derived from measurements, DFT calculations and XRD simulations, respectively, for specific bilayer compositions (given in numbers of monolayers) and arranged in order of increasing FeCo content. In the DFT calculations, pure Fe layers were used. Included are also the nominal $\langle a \rangle$ as well as the measured $\langle a \rangle$ and $\langle c \rangle$ values.

Bilayer composition	Exp. $(c/a)_{FC}$	DFT $(c/a)_{FC}$	Sim. $(c/a)_{FC}$	Nominal $\langle a \rangle$ (Å)	Exp. $\langle a \rangle$ (Å)	Exp. $\langle c \rangle$ (Å)
3 FeCo/7 Pt	1.18(3)	1.22		2.792	2.69	3.87
6 FeCo/9.5 Pt	1.26(3)			2.798	2.71	3.84
4 FeCo/6 Pt	1.24(3)		1.28(1)	2.799	2.69	3.83
3 FeCo/3 Pt	1.31(3)	1.21		2.806	2.65	3.88
5 FeCo/5 Pt	1.28(3)			2.806	2.72	3.79
8 FeCo/8 Pt	1.25(3)			2.806	2.70	3.75
8 FeCo/6 Pt	1.28(3)			2.811	2.66	3.76
6 FeCo/4 Pt	1.27(3)		1.32(1)	2.813	2.67	3.73
7 FeCo/3 Pt	1.28(3)	1.18		2.819	2.68	3.67

the 4/6 and 6/4 samples are 1.28 ± 0.01 and 1.32 ± 0.01, respectively. This is in reasonable agreement with the results from the simple c/a calculations described above. Also, the change in the Pt volume is only about 0.5–1.5%, further supporting the assumptions about the elastic response in Pt.

Density functional theory (DFT) calculations were performed to optimize the structural properties of some specific superlattice compositions n_{FC}/n_{Pt}. The optimization of the c/a ratio and internal coordinates were performed by the plane wave code (VASP) [27, 28] within the projector augmented wave (PAW) [29] method. A kinetic energy cut-off of 500 eV was used for the plane waves included in the basis set. The exchange correlation potential was treated in the generalized gradient approximation (GGA) [30]. Hellmann–Feynman forces were calculated with a tolerance of 0.01 eV $Å^{-1}$. For Brillouin zone integration, a $6 \times 6 \times 2$ special k-point grid was used in the Monkhorst–Pack scheme [31]. The c/a results are presented together with experimental values in table 2. The atomic positions obtained in the optimized structure were further used to justify the assumption, about the preserved Pt volume, that was made in the calculation of experimental c_{Pt} and c_{FC}, as described above. The volumes per atom in each monolayer in the 3/7, 3/3 and 7/3 supercells were calculated. It was found that the volume difference between the 3/7 and 7/3 samples was on the order of 8% per Fe atom, but below 1% per Pt atom. Thus the density functional calculations and XRD simulations agree on the elastic response in the Pt layers.

Also presented in table 2 are the nominal average lattice parameters, $\langle a \rangle$, obtained from equation (1) with the nominal number of monolayers and bulk lattice parameters of the constituents, as well as the experimental $\langle a \rangle$ and $\langle c \rangle$ values from the XRD measurements. The agreement between theoretical and experimental c/a values is acceptable for the 3/7 sample but rather poor for the 3/3 and 7/3 samples. One reason for this could be the use of the same experimental in-plane a_{FC}, obtained from measurements on the 3/7 sample, for all three samples in the DFT calculations.

4.2. Structural quality

In the TEM micrograph, figure 7, a number of dislocations and sections with slightly tilted layers are visible. Combining this with the (103) RSM data for the same sample (6/9.5), we can compare structural quantities, e.g. the dislocation density from the micrograph and the lateral correlation length, $\zeta_{\parallel}$, from RSM. The broadening of x-ray scattering peaks has its origin

both in the correlation lengths and in the sample mosaicity. The contributions can be separated from each other in reflections from atomic planes inclined to the sample surface [22, 32]. The mosaicity causes smearing in a direction perpendicular to the scattering vector, whereas the broadening due to finite $\zeta_{\parallel}$ will be parallel to the surface plane.

The full widths at half maximum (FWHM) along the Q_x and Q_z directions, as defined in figure 4, of the (103) superlattice reflection were extracted using the Philips X'Pert Epitaxy software. Using Fewster's method [22, 32] a lateral correlation length $\zeta_{\parallel} \approx 830$ Å was obtained for the 6/9.5 sample. This is the same order of magnitude as the grain size seen in the TEM micrograph, with approximately ten distinct grains across the lateral length of 1800 Å. We also extracted the perpendicular correlation length, $\zeta_{\perp} \approx 110$ Å, from the superlattice (002) reflection using the Scherrer formula [33]. The mosaicity calculated from the (103) peak widths is 1.23°, agreeing with the FWHM of the (002) peak rocking curve [34], which for this sample is 1.26°.

Looking at the variation of average in-plane lattice parameters in figure 6, there are no significant changes in $\langle a \rangle$ with FeCo content. However, it should be noted from both figure 6 and table 2 that all $\langle a \rangle$ values are smaller than expected from the bulk values of FeCo (bcc $a_0 = 2.84$ Å [35]) and Pt (bct $a_0 = 2.77$ Å, $c_0 = 3.92$ Å). This cannot be a substrate-related effect, since the lattice parameter of MgO is larger than both Fe and Pt. There are two possible scenarios, both resulting in a lowering of the in-plane lattice parameter: stabilization of fcc FeCo (bct $a_0 = 2.49$ Å, $c_0 = 3.52$ Å), or that there is a region of interdiffusion between the FeCo and Pt layers. As seen from the solid line in figure 6, an fcc alloy of Fe and Pt will always have a smaller in-plane (bct) lattice parameter than Fe in the bcc phase and Pt in the fcc phase.

By comparing the surface segregation energies of the elements, E_{segr}, it is possible to estimate if the interfaces have a tendency to interdiffuse [36, 37]. In the following, a negative E_{segr} will indicate a stable interface, and consequently a positive E_{segr} will indicate interdiffusion. In the data presented by Ruban and coworkers [37], pure Fe and Co on (100) Pt were found to be have a tendency towards interdiffusion, $E_{\text{segr}}^{\text{Fe/Pt}} = 0.37$ eV and $E_{\text{segr}}^{\text{Co/Pt}} = 0.55$ eV. On the other hand, Pt on (100) bcc Fe was found to be stable, $E_{\text{segr}}^{\text{Pt/Fe}} = -0.78$ eV. Unfortunately, the data do not contain any values for Pt on (100) bcc Co, although Pt on (0001) hcp Co is an energetically stable interface with $E_{\text{segr}}^{\text{Pt/Co}} = -0.38$ eV. The calculations in [37] do not take into account the growth temperature or any formation of intermetallic phases that can occur during interdiffusion. However, they point to the fact that the FeCo-on-Pt interface could be interdiffused, while the Pt-on-FeCo interface should not be.

X-ray reflectivity simulations give rather small interface widths, typically 2.6 Å on one interface and 1.3 Å on the other (which interface is wider cannot be determined from the simulations). An example of a simulated composition profile for the thick 8/8 sample, figure 10, does however show that even this sample consists mostly of interface regions. Samples with even smaller thicknesses of FeCo will consequently never attain pure interior regions in the FeCo layers. The asymmetric interface widths could indicate that one of the interfaces is interdiffused, although specular reflectivity measurements cannot distinguish between the roughness and interdiffusion contributions to the interface widths [38]. Thus, to resolve this issue, further studies are necessary, e.g. by off-specular reflectivity which only probes the roughness. Interdiffusion is of course of particular interest, since it has potentially large effects on the magnetocrystalline anisotropy; in particular, FePt is strongly anisotropic [6], as mentioned in the introduction. Effects of induced Pt polarization will also be addressed in future experiments.

It is suggested by figure 7 that, closer to the substrate, the dislocations are more dense. The defects are seen especially clearly as white vertical streaks in the Pt buffer layer in the

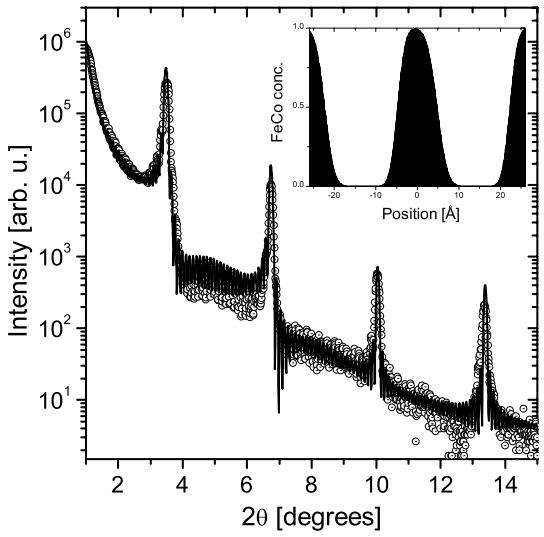

Figure 10. The figure shows the measured x-ray reflectivity for the 8/8 sample (circles) together with the best fit (full line). The inset shows the average composition profile used in the fit (note that it is not symmetric around the zero position). See text for details.

enlarged inverted portion. This has to do with the deposition procedure and gradual removal of the misfit between substrate and superlattice. Thus, the crystalline quality should be improved by making samples with increased total thickness, or by choosing a substrate with a matching lattice parameter.

5. Conclusions

An extensive study of the growth and structural properties of $Fe_{0.36}Co_{0.64}$/Pt(001) superlattices, grown by sputtering at 200 °C, has been performed. Special effort was put into investigating the c/a ratio in the Fe–Co layers, since this is of immediate interest for the interpretation of magnetic properties. It was shown that Fe–Co/Pt superlattices grow epitaxially on MgO(001) substrates with a buffer layer of Fe and Pt. The Fe–Co lattice is distorted into a body centred tetragonal structure with c/a values in the range 1.18–1.31. The derivation of $Fe_{0.36}Co_{0.64}$ lattice parameters from the measured averages was supported by independent density functional calculations. Lateral and perpendicular correlation lengths were found to be 830 and 110 Å, respectively, with the x-ray diffraction results corroborating transmission electron micrographs. The interface width is about two monolayers, according to x-ray reflectivity simulations. The overall defect density can probably be decreased by increasing the number of bilayers in the stack.

Acknowledgments

Financial support from the Swedish Foundation for Strategic Research (SSF), the Swedish Research Council (VR), the Royal Physiographic Society in Lund and the Göran Gustafsson Foundation is gratefully acknowledged. We would also like to thank Ola Wilhemsson for assistance with the XPS measurements, as well as Klaus Leifer, Till Burkert and Olle Eriksson for discussions.

References

[1] Thompson D A and Best J S 2000 *IBM J. Res. Dev.* **44** 311
[2] Weller D and Moser A 1999 *IEEE Trans. Magn.* **35** 4423
[3] Weller D, Moser A, Folks L, Best M E, Lee W, Toney M F, Schwickert M, Thiele J-U and Doerner M F 2000 *IEEE Trans. Magn.* **36** 10
[4] Burkert T, Eriksson O, James P, Simak S I, Johansson B and Nordström L 2004 *Phys. Rev.* B **69** 104426
[5] Burkert T, Nordström L, Eriksson O and Heinonen O 2004 *Phys. Rev. Lett.* **93** 027203
[6] Lairson B M and Clemens B M 1993 *Appl. Phys. Lett.* **63** 1438
[7] Burkert T, Eriksson O, Simak S I, Ruban A V, Sanyal B, Nordström L and Wills J M 2005 *Phys. Rev.* B **71** 134411
[8] Martins A, Fantini M C A, Souza-Neto N M, Ramos A Y and Santos A D 2006 *J. Magn. Magn. Mater.* **305** 152
[9] Shima T, Moriguchi T, Seki T, Mitani S and Takanashi K 2003 *J. Appl. Phys.* **93** 7238
[10] Andersson G, Burkert T, Warnicke P, Björck M, Sanyal B, Chacon C, Zlotea C, Nordström L, Nordblad P and Eriksson O 2006 *Phys. Rev. Lett.* **96** 037205
[11] Hellwege K-H and Hellwege A M (ed) 1971 *Numerical Data and Functional Relationships in Science and Technology* (*Landolt–Börnstein New Series* vol 6) (Berlin: Springer)
[12] Sakurai M 1994 *Phys. Rev.* B **50** 3761
[13] Sakurai M, Imamura N, Hirano K and Shinjo T 1995 *J. Magn. Magn. Mater.* **147** 16
[14] Han K, Yu-Zhang K, Kung H, Embury J D, Daniels B J and Clemens B M 2002 *Phil. Mag.* A **82** 1633
[15] Daniels B J, Nix W D and Clemens B M 1995 *Appl. Phys. Lett.* **66** 2969
[16] Warnicke P, Andersson G, Björck M, Ferré J and Nordblad P 2006 unpublished
[17] Isberg P, Svedberg E B, Hjörvarsson B, Wäppling R and Hultman L 1997 *Vacuum* **48** 483
[18] Mewes T, Rickart M, Mougin A, Demokritov S O, Fassbender J, Hillebrands B and Scheib M 2001 *Surf. Sci.* **481** 87
[19] Björck M, Andersson G, Lindgren B, Wäppling R, Stanciu V and Nordblad P 2004 *J. Magn. Magn. Mater.* **284** 273
[20] Nordling C and Österman J 1987 *Physics Handbook* (Lund: Studentlitteratur)
[21] Doolittle L R 1985 *Nucl. Instrum. Methods Phys. Res.* B **15** 227
[22] Fewster P F 2003 *X-Ray Scattering from Semiconductors* (London: Imperial College Press)
[23] Birch J, Sundgren J-E and Fewster P F 1995 *J. Appl. Phys.* **78** 6562
[24] Schuller I K, Grimsditch M, Chambers F, Devane G, Vanderstraeten H, Neerinck D, Locquet J-P and Bruynseraede Y 1990 *Phys. Rev. Lett.* **65** 1235
[25] Kittel C 1996 *Introduction to Solid State Physics* (New York: Wiley)
[26] Fullerton E E, Schuller I K, Vanderstraeten H and Bruynseraede Y 1992 *Phys. Rev.* B **45** 9292
[27] Kresse G and Hafner J 1993 *Phys. Rev.* B **47** 558
[28] Kresse G and Furthmüller J 1996 *Phys. Rev.* B **54** 11169
[29] Blöchl P E 1994 *Phys. Rev.* B **50** 17953
[30] Perdew J P and Yang Y 1992 *Phys. Rev.* B **45** 13244
[31] Monkhorst H J and Pack J D 1976 *Phys. Rev.* B **13** 5188
[32] Fewster P F 1996 *Rep. Prog. Phys.* **59** 1339
[33] Granberg P, Isberg P, Svedberg E B, Hjörvarsson B, Nordblad P and Wäppling R 1998 *J. Magn. Magn. Mater.* **186** 154
[34] Cullity B D 1978 *Elements of X-Ray Diffraction* (Reading, MA: Addison-Wesley)
[35] Wijn H P J (ed) 1991 *Data in Science and Technology. Magnetic Properties of Metals: d-Elements, Alloys and Compounds* (Berlin: Springer)
[36] Christensen A, Ruban A V, Stoltze P, Jacobsen K W, Skriver H L, Nørskov J K and Besenbacher F 1997 *Phys. Rev.* B **56** 5822
[37] Ruban A V, Skriver H L and Nørskov J K 1999 *Phys. Rev.* B **59** 15990
[38] Pape I, Hase T P A, Tanner B K and Wormington M 1998 *Physica* B **253** 278